Strain localization and failure load predictions of geosynthetic reinforced soil structures

Mustafa Alsaleh[†]

Virtual Product Development Division, Caterpillar Inc., 14009 Old Galena Rd., Mossville, IL 61552, U.S.A.

Akadet Kitsabunnarat[‡]

HNTB, 11414 W. Park Place, Milwaukee, WI 53224, U.S.A.

Sam Helwany[†‡]

Department of Civil Engineering and Mechanics, University of Wisconsin at Milwaukee, 3200 North Cramer St., EMS W230 Milwaukee, WI 53201, U.S.A.

Abstract. This study illustrates the differences between the elasto-plastic cap model and Lade's model with Cosserat rotation through the analyses of two large-scale geosynthetic-reinforced soil (GRS) retaining wall tests that were brought to failure using a monotonically increasing surcharge pressure. The finite element analyses with Lade's model were able to reasonably simulate the large-scale plane strain laboratory tests. On average, the finite element analyses gave reasonably good agreement with the experimental results in terms of global performances and shear band occurrences. In contrast, the cap model was not able to simulate the development of shear banding in the tests. In both test simulations the cap model predicted failure loads that were substantially less than the measured ones.

Keywords: geosynthetic-reinforced soil; GRS; geogrids; geotextile; Lade's single hardening model; cosserat rotation; druker-prager cap model; failure surface; shear band; failure load; elasto-plastic.

1. Introduction

The cap plasticity model has been widely used in finite element analysis programs for a variety of geotechnical engineering applications (e.g. Nelson and Baladi 1977, Baladi and Rohani 1979, Chen and McCarron 1983, Minuzo and Chen 1984, Daddazio *et al.* 1987, McCarron and Chen 1987). The cap model can reasonably describe soil behavior because it is capable of considering the effect of stress history, stress path, and the effect of the intermediate principal stress (Huang and Chen 1990). It is important to note, however, that the cap model embodies a two-invariant formulation

---

† Ph. D., Senior Research and Development Engineer, E-mail: Alsaleh_Mustafa_I@cat.com
‡ Ph. D., Geotechnical Engineer, E-mail: akitsabunnarat@hntb.com
†‡ Professor, Corresponding Author, E-mail: helwany@uwm.edu

that does not account for dilatancy. The dilatancy phenomenon can be important when characterizing the behavior of compacted soils, and that can be achieved using soil models with three-invariant formulation (e.g. Lade and Nelson 1987) that are suited for detecting stress localization (shear banding) synonymous with failure. In geosynthetic-reinforced soil structures the presence of geosynthetic inclusions within the compacted soil may hinder the growth of the shear band. More experience using such models for dilative soils with geosynthetic inclusions is desired.

Numerous researchers have attempted to calculate the failure loads of geosynthetic-reinforced soil (GRS) retaining walls using nonlinear-elastic and elasto-plastic soil models with various degrees of success. In a unique study, Lai *et al*. (2003) were successful in analyzing a GRS retaining wall using the finite element method with Lade's elasto-plastic model and provisions for shear banding. The present study will illustrate the differences between the elasto-plastic cap model and Lade's model with Cosserat rotation through the analyses of two large-scale GRS retaining wall tests that were brought to failure using a monotonically increasing surcharge pressure.

First, a finite element analysis with Lade's elasto-plastic soil model and Cosserat theory is carried out to show that the finite element method is capable of realistically simulating the behavior of GRS retaining walls and calculating their failure loads with reasonable accuracy. Lade's elasto-plastic constitutive model (Kim and Lade 1988, Lade and Kim 1988) along with Cosserat rotation (Cosserat 1909), suited for detection of strain localization, is used for the analysis of two geosynthetic-reinforced soil retaining walls: the RMC wall performed at the Royal Military College of Canada and the Denver wall performed at the University of Colorado at Denver. These two large-scale laboratory test walls were chosen because they were subjected to surcharge pressures until failure upon which failure surfaces were developed within their reinforced zones. These failure surfaces were accurately measured and documented (Bathurst *et al*. 1987, Wu 1992).

Second, the elasto-plastic cap model is used for the analysis of the aforementioned GRS retaining walls: the RMC wall and the Denver wall. The performance of the cap model is then compared with that of Lade's model with Cosserat rotation in term of their predictions of facing deformations, geosynthetic strains, shear banding, and consequently, the failure loads.

2. Lade's single hardening model (SHM) and cosserat rotation

It has been acknowledged by many researchers that classical continuum mechanics laws fail to describe the phenomenon of strain localization that takes place prior to failure in soils. This drawback is due to the fact that the mathematical solution is ill posed and the numerical solution is highly dependent on the discretization resolution. Therefore, an internal length scale is needed to regularize the strain field and smoothly pass through the localization zones. Such length scales can be accommodated into a micromechanical based formulations. Unfortunately, such formulations don't exist in the shape that can be implemented into a finite element solution yet. However, macro or continuum based formulations can be enhanced through either Cosserat theory or high order gradient theories to accommodate the proper internal length scales. This way the solution becomes less sensitive to the mesh size when performing a finite element analysis. Lade's single hardening constitutive model for soils has been enhanced to incorporate internal length scales and some other micromechanical parameters though Cosserat rotation (Cosserat 1909). The model was implemented into the commercial finite element program ABAQUS® using User Element utility subroutine (Alsaleh *et al*. 2006, Alshibli *et al*. 2006). Lade's model is described in details in the papers by Kim

and Lade (1988) and Lade and Kim (1988).

A brief description of Lade's soil model is presented herein. This model is an elasto-plastic soil model with a single yield surface expressed in terms of stress invariants. The hardening parameter in this model is assumed to be the total plastic work (i.e. the plastic work done by shear strains and volumetric strains), which is used to define the evolution of the yield surface. The model involves 11 parameters that can be determined from three CD triaxial compression tests and one isotropic compression test.

The total strain increments are divided into elastic and plastic strain components:

$$d\varepsilon = d\varepsilon^e + d\varepsilon^p \tag{1}$$

For a given *effective* stress increment the elastic and plastic strain components are calculated separately, the elastic strains by a nonlinear form of Hooke's law and the plastic strains by a plastic stress-strain law.

The elastic strain increments are calculated using Eq. (2) that accounts for the nonlinear variation of Young's modulus with stress state (Lade and Nelson 1987):

$$E = Mp_a\left[\left(\frac{I_1}{p_a}\right)^2 + 6\frac{1+v}{1-2v}\left(\frac{J'_2}{p_a^2}\right)\right]^\lambda \tag{2}$$

where, v is Poisson's ratio, I_1 is the first invariant of the stress tensor, J'_2 is the second invariant of the deviatoric stress tensor, p_a is the atmospheric pressure expressed in the same units as E, I_1 and J'_2, M is the modulus number and λ is the exponent. Both M and λ are dimensionless constants. The parameters M, λ, and v can be determined from the unloading-reloading cycles of triaxial compression tests.

In Lade's model, the relationship of stresses at failure (failure criterion) is expressed in terms of the first and third stress invariants, I_1 and I_3:

$$f_n = \left(\frac{I_1^3}{I_3} - 27\right)\left(\frac{I_1}{p_a}\right)^m \tag{3a}$$

$$f_n = \eta_1 \text{ at failure} \tag{3b}$$

The parameters η_1 and m are dimensionless constants that can be determined from triaxial compression test results.

Plastic flow occurs when the state of stress touches the yield criterion f_n causing the material to undergo plastic deformations. The plastic strain increments are calculated from the flow rule:

$$d(\varepsilon)^p = d\lambda_p \frac{dg_p}{d(\sigma)} \tag{4}$$

where: I_3 is the third invariant of the stress tensor, (σ) is the stress tensor, $(\varepsilon)^p$ is the plastic component of the total strain tensor (ε), λ_p is the proportionality factor (a positive scalar), and g_p is the plastic potential function given as:

$$g_p = \left(\psi_1\frac{I_1^3}{I_3} - \frac{I_1^2}{I_2} + \psi_2\right)\left(\frac{I_1}{p_a}\right)^\mu \tag{5}$$

where: I_2 is the second stress invariant, ψ_2 and μ are material parameters that can be determined from the results of triaxial compression tests, ψ_1 is a parameter related to the curvature parameter

m of the failure criterion as suggested by Kim and Lade (1988):

$$\psi_1 = 0.00155 \cdot m^{-1.27} \tag{6}$$

The parameter ψ_2 controls the intersection of the plastic potential with the hydrostatic pressure axis, while the exponent μ determines the curvature of the plastic potential in the principal stress space.

Lade and Kim (1988) employed an isotropic yield function given as:

$$f_p = f'_p(I_1, I_2, I_3) - f''_p(W_p) = 0 \tag{7}$$

Where

$$f'_p = \left(\psi_1 \frac{I_1^3}{I_3} - \frac{I_1^2}{I_2} \right) \left(\frac{I_1}{p_a} \right)^h e^q \tag{8}$$

The parameter h in Eq. (8) is determined based on the assumption that the plastic work is constant along a yield surface. Define the stress level as:

$$S = \frac{f_n}{\eta_1} = \frac{1}{\eta_1} \left(\frac{I_1^3}{I_3} - 27 \right) \left(\frac{I_1}{p_a} \right)^m \tag{9}$$

in which f_n is given by Eq. (3a), and η_1 is the value of f_n at failure (Eq. 3b). The stress level S varies from zero at the hydrostatic pressure axis to unity at the failure surface (i.e. $f_n = \eta_1$). The parameter q (Eq. 8) varies with S as follows:

$$q = \frac{\alpha S}{1 - (1 - \alpha)S} \tag{10}$$

where α is a constant that can be determined by fitting Eq. (10) to the results of triaxial compression tests.

Work hardening occurs when the yield surface expands isotropically as the plastic work increases:

$$f''_p = \left(\frac{1}{D} \right)^{\frac{1}{\rho}} \left(\frac{W_p}{p_a} \right)^{\frac{1}{\rho}} \tag{11}$$

where ρ and D are constants. This means that f''_p increases only if the plastic work increases. D and ρ are given as:

$$D = \frac{C}{(27\psi_1 + 3)^\rho} \tag{12}$$

and

$$\rho = \frac{p}{h} \tag{13}$$

The parameters C and p in Eqs. (12) and (13) can be estimated from the results of an isotropic compression test by best fitting Eq. (14) with the test results:

$$W_p = Cp_a \left(\frac{I_1}{p_a} \right)^p \tag{14}$$

The yield surface is similar in shape to the failure surface. When a stress increment is applied, the plastic work increases and the isotropic yield surface expands until the current stress state hits the failure surface.

For work softening, the yield surface contracts isotropically as such:

$$f''_p = A e^{-B\frac{W_p}{P_a}} \tag{15}$$

The constants A and B can be calculated from the value of f''_p and the slope of the hardening curve at the point of peak failure at which $S = 1$.

The relationship between the plastic work increment and the proportionality factor $d\lambda_p$ (Eq. 4) can be expressed in terms of the plastic potential g_p as:

$$d\lambda_p = \frac{dW_p}{\mu g_p} \tag{16}$$

The increment of plastic work in Eq. (16) can be calculated by differentiation of the hardening equation and the softening equation.

3. Cosserat rotation and internal length scale

According to Alsaleh (2004), Bauer and Huang (2001), Huang *et al.* (2002), Vardoulakis and Sulem (1995), Gudehus and Nubel (2004), Pasternak and Mühlhaus (2002), Rubin (2000), Tejchman and Bauer (1996), and Tomantschger (2002), the additional degree of freedom, which is the Cosserat rotation is employed in the formulation to capture the effect of particle micro-rotation and enable incorporating an internal length scale in granular materials modeling.

The Green or the Lagrangian strain tensor can be decomposed into linear and non-linear components as:

$$E_{ij} = {}^n e_{ij} + {}^n \eta_{ij} \tag{17a}$$

$$^n e_{ij} = \frac{1}{2}(u_{i,j} + u_{j,i}) \tag{17b}$$

and;

$$^n \eta_{ij} = \frac{1}{2}(u_{k,i} u_{k,j}) \tag{17c}$$

The definition of the quantity $u_{i,j}$ is the displacement field derivative with respect to the current position and;

$$\dot{e}_{ij} = D_{ij} = \frac{1}{2}(v_{i,j} + v_{j,i}) \tag{17d}$$

Cosserat continuum is composed of individual particles and each particle will deform in translation and rotation based on the interaction between a specific particle and the neighboring. The spin or the rotation of the particle can be described by ω^c, which means the Cosserat or material point rotation; this rotation can be defined as a vector similar to the displacement vector, u_i. Then

one might define vector as $\omega_i^c = \omega^c$. The objective or Cosserat strain rate tensor now can be redefined as:

$$_{n}^{n+1}\dot{\gamma}_{ij} = {}_{n}^{n+1}\dot{E}_{ij} + {}^{n}\dot{\chi}_{ij} \tag{18a}$$

and;

$$^{n}\dot{\chi}_{ij} = {}^{n}\dot{\Omega}_{ij} - {}^{n}\dot{\Omega}_{ij}^{c} \tag{18b}$$

where, Ω and Ω^c are defined below and $\{\dot{\gamma}\}$ is defined here as the spatial objective strain rate tensor. The strain rate tensor defined in Eq. (18) produces non-symmetry in the stress tensor. The curvature vector of deformation or the gradient of particle rotation can be defined as:

$$^{n}\kappa_i = {}^{n}\omega_{j,i}^{c} \tag{19a}$$

where Eq. (19a) will reduce into the following form for plane-strain case:

$$^{n}\kappa_i = \omega_{3,i}^{c} \qquad i = 1, 2 \tag{19b}$$

Eq. (18) shows that there is one type of strain rate and two types of spin tensor, those are the classical strain - rate tensor, $\dot{E}_{ij}$, and the classical spin tensor:

$$^{n}\dot{\Omega}_{ij} = \frac{1}{2}(v_{i,j} - v_{j,i}) \tag{20}$$

and the Cosserat spin tensor that can be written as:

$$\Omega_{ij}^{c} = -e_{ijk}\omega_k^{c} \tag{21a}$$

where e_{ijk} is the Ricci permutation tensor and again for a plane-strain problem (21a) will collapse into:

$$^{n}\Omega_{ij}^{c} = -e_{ij3}\omega_3^{c} \tag{21b}$$

Lade's model is a stress-invariant dependent model that requires all three stress invariants to update all state variables. The second stress invariant was rewritten to accommodate the couple stresses as follow:

$$I_{II} = h_1[\sigma_{12}\sigma_{21} - \sigma_{11}\sigma_{22} - \sigma_{11}\sigma_{33} - \sigma_{22}\sigma_{33}] - h_2\frac{m_1 m_2}{l_s^2} \tag{22}$$

where,

h_1 and h_2 are weighing factors ($h_1 = \frac{1}{2}$ and $h_2 = 1$ are used in the present study).
Vardoulakis and Sulem (1995) have used similar approach to modify stress second invariant;
m_1 and m_2 are couple stresses and
l_s is an internal length scale (= mean particle size d_{50}).
In a plane strain Cosserat continuum and for simplicity in finite element implementation, the stress matrix can be expressed in the following vector (Eq. (23a)).

$$\{\sigma\} = \{\sigma_{11} \ \sigma_{22} \ \sigma_{33} \ \sigma_{13} \ \sigma_{31} \ m_1/l_s \ m_3/l_s\} \tag{23a}$$

The strain matrix for 2D Cosserat continuum can be expressed in a vector form as:

$$\{\gamma\} = \{\gamma_{11} \ \gamma_{22} \ \gamma_{33} \ \gamma_{13} \ \gamma_{31} \ l_a\kappa_1 \ l_a\kappa_3\} \tag{23b}$$

where; l_a, is the length of the arm of rotation. This is done in an attempt to separate two different

length scales, one is the contact surface and the other is the arm of rotation.

It is more convenient to deal with time rates for stresses and strains as such:

$$\{\dot{\sigma}\} = [\mathbf{D}]\{\dot{\gamma}\} \tag{24}$$

where, $[\mathbf{D}]$ is the elasto-plastic stiffness matrix derived within Cosserat continuum.

Moreover, the micro-structural properties (particle shape, surface roughness and size) have been incorporated into the model through the internal length scale quantity. Alsaleh (2004) showed that the solution for the shear band thickness is not highly dependent on the element size because of the non-local theory employed. A lower limit for the element-to-internal length scale size ratio of about 4-6 is recommended. Higher ratios can be used and can provide same level of accuracy at lower computational cost.

4. Cap model

The Drucker-Prager/Cap plasticity model has been widely used in finite element analysis programs for a variety of geotechnical engineering applications because it is capable of considering the effect of stress history, stress path, and the effect of the intermediate principal stress. The yield surface of the modified Drucker-Prager/Cap plasticity model consists of three parts: a Drucker-Prager shear failure surface, an elliptical "cap," which intersects the mean effective stress axis at a right angle, and a smooth transition region between the shear failure surface and the cap.

The elastic behavior is modeled as linear elastic using the generalized Hooke's law. The onset of the plastic behavior is determined by the Drucker-Prager failure surface and the cap yield surface. The Drucker-Prager failure surface is given by:

$$F_s = t - p\tan\beta - d = 0 \tag{25}$$

where β is the soil's angle of friction and d is its cohesion in the p-t plane. In this equation t is a measure of shear stress (reduces to stress deviator in a triaxial stress state) and p is the mean effective stress.

The cap yield surface is an ellipse with eccentricity $= R$ in the p-t plane. The cap yield surface is dependent on the third stress invariant. The cap surface hardens (expands) or softens (shrinks) as a function of the volumetric plastic strain. When the stress state causes yielding on the cap, volumetric plastic strain (compaction) results causing the cap to expand (hardening). But when the stress state causes yielding on the Drucker-Prager shear failure surface, volumetric plastic dilation results causing the cap to shrink (softening). The cap yield surface is given as:

$$F_c = \sqrt{(p - p_a)^2 + \left[\frac{Rt}{(1 + \alpha - \alpha / \cos\beta)}\right]^2} - R(d + p_a\tan\beta) = 0 \tag{26}$$

Where, R is a material parameter that controls the shape of the cap, α is a small number (typically 0.01 to 0.05) used to define a smooth transition surface between the Druker-Prager shear failure surface and the cap:

$$F_t = \sqrt{(p - p_a)^2 + \left[t - \left(1 - \frac{\alpha}{\cos\beta}\right)(d + p_a\tan\beta)\right]^2} - \alpha(d + p_a\tan\beta) = 0 \tag{27}$$

p_a is an "evolution parameter" that controls the hardening/softening behavior as function of the

volumetric plastic strain. The hardening/softening behavior is simply described by a piecewise linear function relating the mean effective (yield) stress, p_b, and the volumetric plastic strain, ε_{vol}^{pl}. This function can be easily obtained from the results of one isotropic compression test with unloading/reloading cycles. Consequently, the evolution parameter, p_a, can be calculated as:

$$p_a = \frac{p_b - Rd}{1 + R\tan\beta} \tag{28}$$

For this model, the flow potential surface in the *p-t* plane consists of two parts. In the cap region the plastic flow is defined by a flow potential that is identical to the yield surface, i.e., associated flow. For the Drucker-Prager failure surface and the transition yield surface a nonassociated flow is assumed: the shape of the flow potential in the *p-t* plane is different from the yield surface.

In the cap region the elliptical flow potential surface is given as:

$$G_c = \sqrt{(p - p_a)^2 + \left[\frac{Rt}{(1 + \alpha - \alpha/\cos\beta)}\right]^2} \tag{29}$$

The elliptical flow potential surface portion in the Drucker-Prager failure and transition regions is given as:

$$G_s = \sqrt{[(p_a - p)\tan\beta]^2 + \left[\frac{t}{(1 + \alpha - \alpha/\cos\beta)}\right]^2} \tag{30}$$

The two elliptical portions, G_c and G_s, provide a continuous potential surface. Because of the nonassociated flow used in this model, the material stiffness matrix is not symmetric. Thus, an unsymmetric solver should be used in association with the Cap model.

5. The RMC geosynthetic-reinfoced soil retaining wall

5.1 Analysis of the RMC wall using Lade's model

In this section, the capability of Lade's model/Cosserat theory embodied in a finite element model to capture the collapse mechanism behind a full-scale geosynthetic-reinforced soil wall with a continuous facing panel is illustrated. The Royal Military College (RMC) retaining wall involves a full-scale 3.5-m high GRS wall model with a continuous facing panel in a plane strain condition. The backfill soil is loaded to failure by surface surcharge using an air bag. Details of the full-scale model and experiments are presented by Bathurst and Benjamin (1990). There are several reasons for selecting the RMC wall test as a benchmark test for the present study: the RMC wall is a full-scale plane strain test that represents a real size structure and yields realistic results. The RMC wall test exhibited a distinct failure surface that developed during testing through the reinforced zone. Also, the facing of the RMC wall consisted of a continuous aluminum panel which is easier to analyze than wrap-around and segmental facing types.

The RMC test configuration, finite element mesh, and boundary conditions are shown in Fig. 1. The backfill soil is contained in a 6-m-long, 2.4-m-wide, and 3.6-m-high reinforced concrete box with low friction side walls and a rough concrete bottom. The wall facing consisted of a 3-m-high continuous aluminum panel pinned at the base and supported by external supports until the full depth of the soil behind the wall has been placed and compacted. The geosynthetic reinforcement
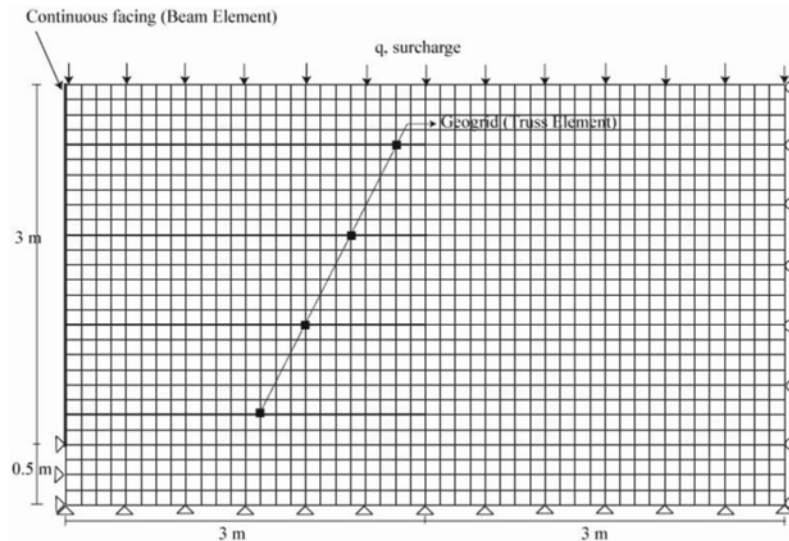
Fig. 1 Finite element mesh of RMC wall

consisted of four layers of 3-m-long geogrid. The backfill material was uniform sand with some fine gravel placed and compacted in 125 mm lifts. The surcharge pressure was applied on top of the backfill in increments of 10 kPa with a 100-h-duration each. Failure occurred in the reinforced soil zone during the 80-kPa loading increment. Inspection revealed a failure scarp in the soil approximately 1 m behind the top of the wall; the surface of the faulted soil mass was observed to have dropped approximately 65 mm. Careful excavation of the backfill revealed a clear failure plane with a log-spiral shape and a ruptured upper layer of geogrid at the connection with the facing.

A 4-node isoparametric plane strain element with four integration points is used for the sand, a 2-node beam element is used for the wall, and a 2-node truss element is used for the geosynthetic reinforcement. The base of the sand layer is fixed in all directions. The right hand side boundary of the sand layer is fixed in the horizontal direction but free in the vertical direction. The backfill soil and the facing panel are interfaced using penalty-type interface elements with an interface friction angle of 20°. The same type of interface is also employed between the soil and the geosynthetic layers.

The backfill soil has a unit weight of $17\,kN/m^3$ and an internal friction angle of 41°. The results of triaxial compression tests carried out on the same sand are shown in Figs. 2a and 2b (Bathurst *et al*. 1987). The dilative behavior of the backfill soil is apparent from the figure, and therefore, the soil is assumed to behave as a dilative elasto-plastic material with the Lade's model parameters, given in Table 1, that were deduced from the triaxial test results, and from the assumed isotropic compression test results shown in Fig. 2c. The isotropic compression test results were taken from a similar soil because of the lack of such test results on the backfill soil of the RMC wall.

Consequent to obtaining Lade's model parameters, the parameters were used to generate the triaxial test results and isotropic compression test results as shown in Fig. 2. The model predictions are compared with the experimental results reported by Bathurst *et al*. (1987) as shown in the same figure.
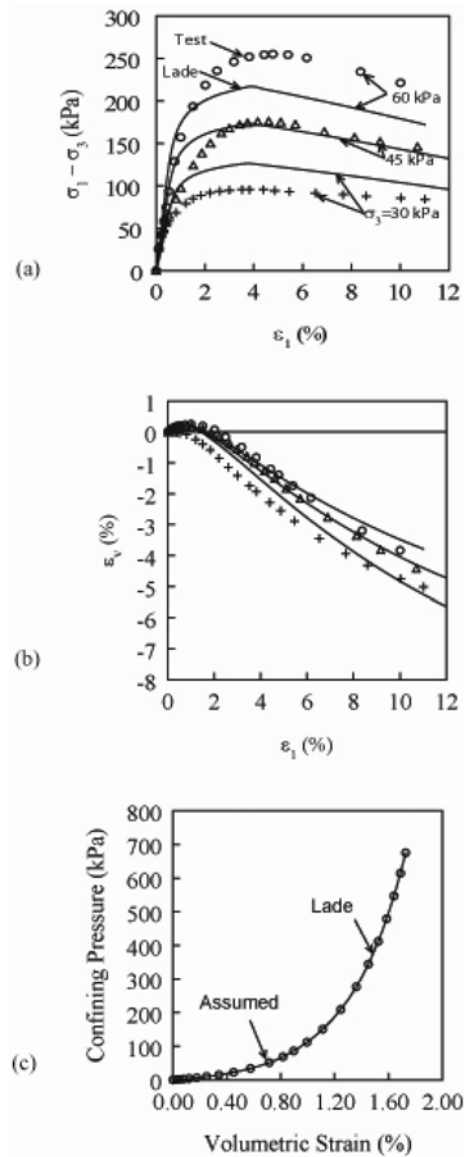
Fig. 2 (a,b) Triaxial test results of backfill sand used in RMC wall; (c) assumed isotropic compression test results

The aluminum facing panel (wall) is assumed to be linear elastic with a cross-dimensional area of $0.025\,\mathrm{m^2/m}$, an elastic modulus of $3\times10^8\,\mathrm{kPa}$, and a shear modulus of $1.25\times10^8\,\mathrm{kPa}$. The geosynthetic reinforcement (Geogrid) has a stiffness (EA) of $204\,\mathrm{kN/m}$ at 2% strain, and an ultimate tensile strength of $12\,\mathrm{kN/m}$ at 14% strain. An elasto-plastic model is used to simulate the geosynthetic behavior.

The finite element analysis of the RMC retaining wall consists of three steps. In Step 1, the gravity load was applied to the sand backfill while the wall was restrained from lateral movement. In Step 2 the lateral restraint of the wall was gradually removed and a one-second rest time was

Table 1 Lade's model parameters for RMC wall

Parameter	Value
Failure Criterion	
m	0.382
η_1	60
Elastic Parameters	
M	120
λ	0.5
υ	0.2
Plastic Potential Function	
ψ_2	-3.1
μ	2.1
Work Hardening Law	
C	0.00005
p	1.4
Yield Function	
α	0.6
h	0.38
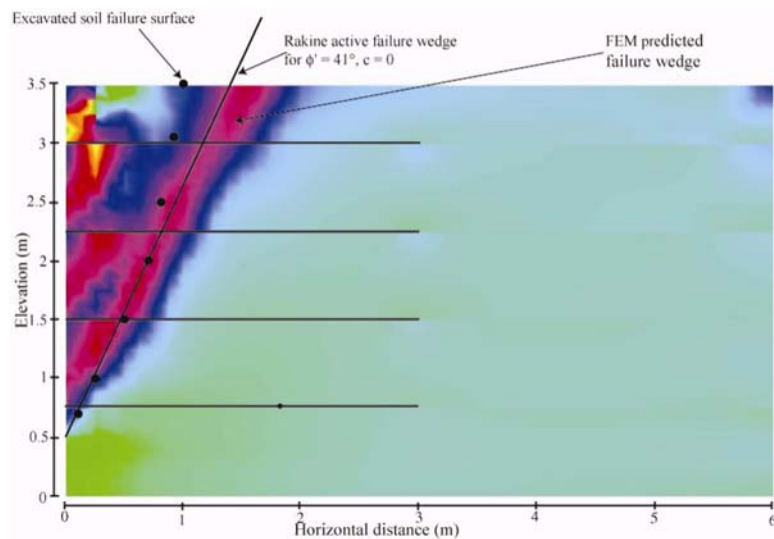
Fig. 3 Failure surfaces: experimental versus numerical results

employed to ensure equilibrium. In Step 3, a monotonically increasing surcharge pressure was applied at the top surface of the backfill soil until failure occurred.

The finite element analysis indicated that failure occurred at a surcharge pressure of approximately 84 kPa. The shear strain contours at failure, shown in Fig. 3, clearly illustrate the presence of a failure plane passing through the heel of the retaining wall and also through the reinforced zone. The experimentally detected failure surface agrees with the predicted one as shown in the same figure. The failure plane predicted by Rankine active earth pressure theory is also
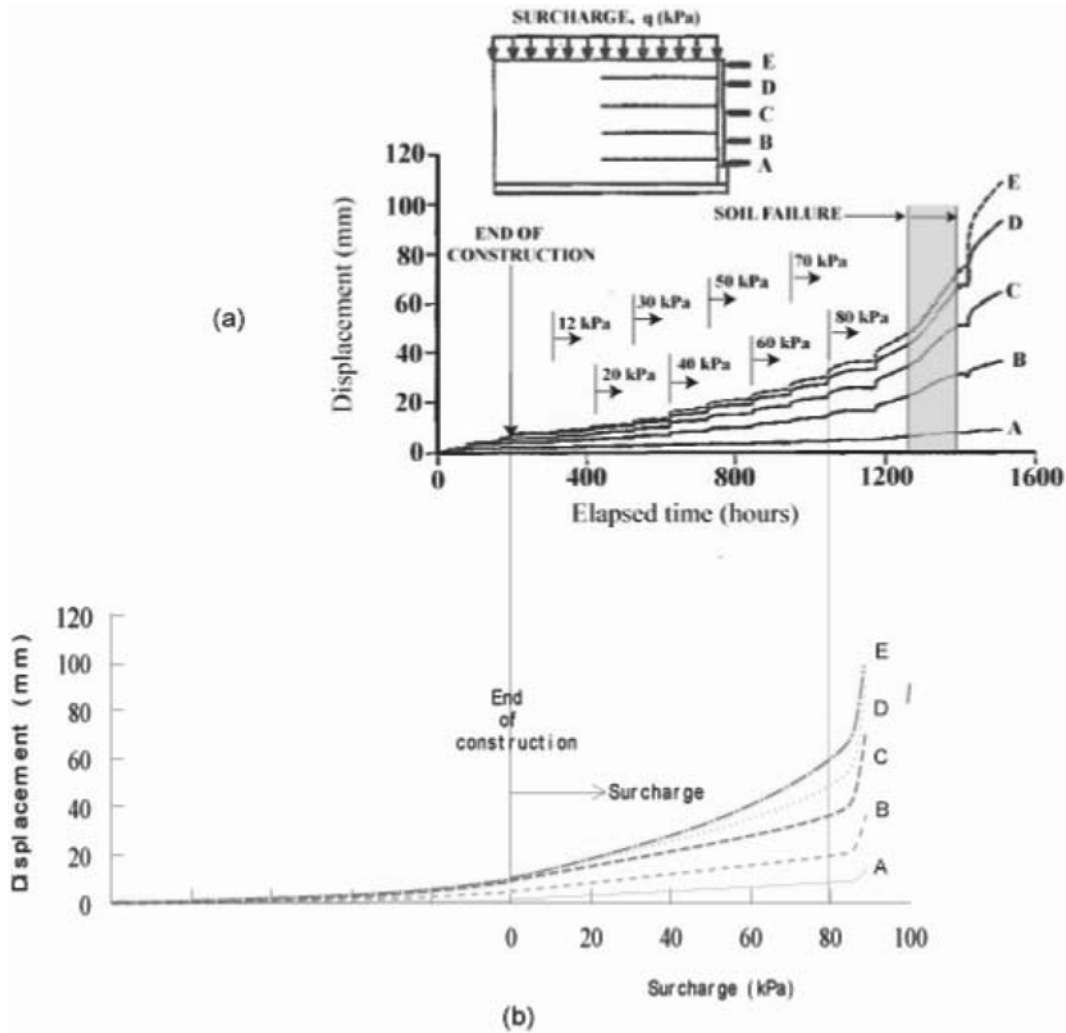
Fig. 4 Wall deformation versus pressure: (a) experimental (after Bathurst and Benjamin 1990), and (b)numerical results

shown in the figure for reference.

Figs. 4a and 4b show respectively the measured and predicted lateral displacements at points A, B, C, D, and E located on the facing panel at different heights. Reasonable agreement is noted between the measured and calculated displacement. Note that the measured results included a 100-h creep period for each 10 kPa surcharge pressure increment. The present finite element analysis neglects creep--the soil model used herein (Lade's model) is time-independent and not suited for creep predictions. Nonetheless, the present finite element model is reasonably capable of predicting the failure load as indicated in Fig. 4b. Finally, Fig. 5 shows comparisons between measured and predicted axial strains in the four reinforcement layers at failure. Reasonable agreement between measured and predicted strains is noted in the figure.
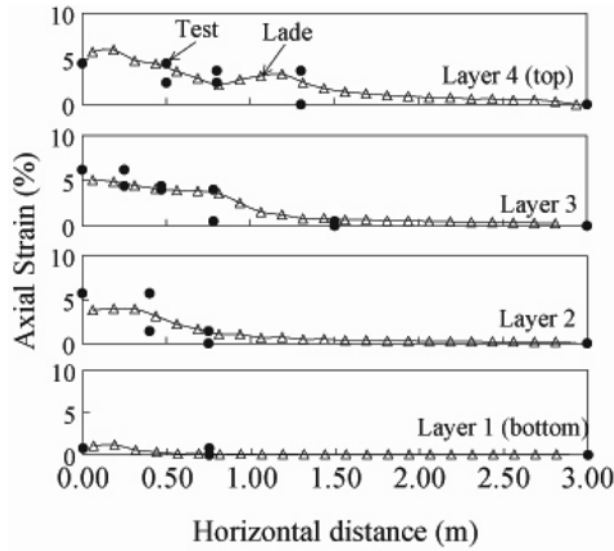
Fig. 5 Strain in geosynthetic layers at failure: experimental versus numerical results

Table 2 Cap model parameters for RMC wall

Elasticity	Plasticity
E = 15000 kPa	d = 1 × 10⁻⁵ kPa
v = 0.2	β = 59.2° for triaxial condition
	β = 47.2° for plane strain condition
	R = 0.2
	Initial Yield = 0.0
	α = 0.1
	K = 1

Yield Stress (kPa)	Volmectric Plastic Strain
2.83	0.000
9.92	0.0005
18.4	0.0011
20	0.0013
26.4	0.0015
30	0.0018
35.4	0.0020
45	0.0021
60	0.0026
100	0.0035
400	0.0043
675	0.0048

5.2 Analysis of the RMC wall using Cap model

The analysis of the RMC wall, described above, is repeated in the exact manner with only one

exception: the cap soil model is used instead of Lade's model with Cosserat rotation. The cap model parameters were obtained from the three triaxial compression tests and the (assumed) isotropic compression test results on the RMC backfill sand. These parameters are given in Table 2. The parameters were used to reproduce the results of the three triaxial compression tests and the isotropic compression test as shown in Fig. 6. The figures indicate good agreement between the cap model and the Lade's model predictions, except for the volumetric strain versus axial strain curves shown in Fig. 6b. As indicated earlier, the cap model is not capable of describing soil dilatancy-it assumes compressive volumetric strains during shearing as indicated in the figure.

The calculated lateral displacement at mid-height of the facing panel of the RMC wall test is
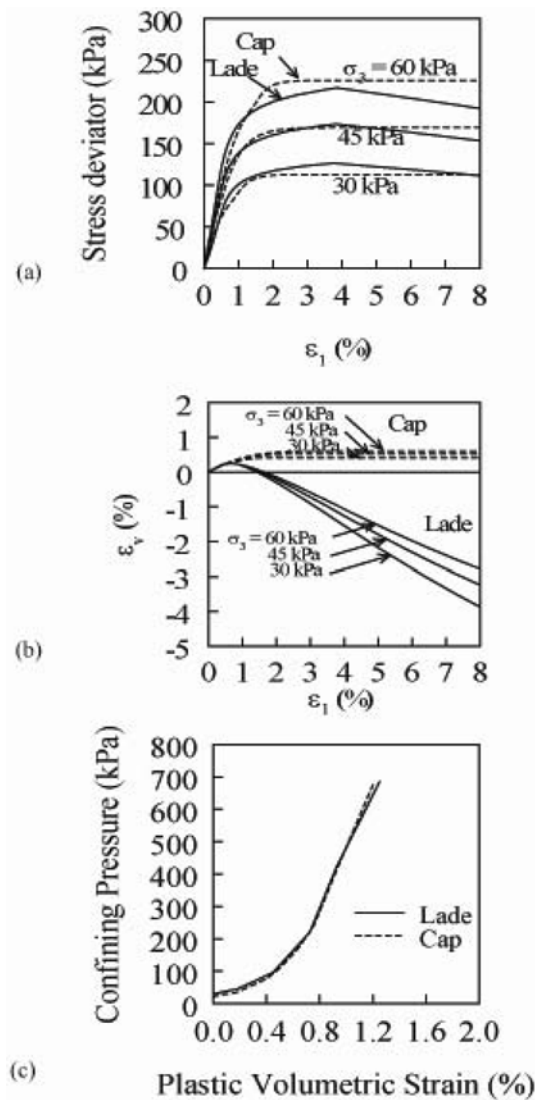
Fig. 6 (a,b) Stress-strain relationship: cap and Lade's models; (c) plastic volumetric strain-confining pressure curves used for the hardening rules of cap and Lade's models
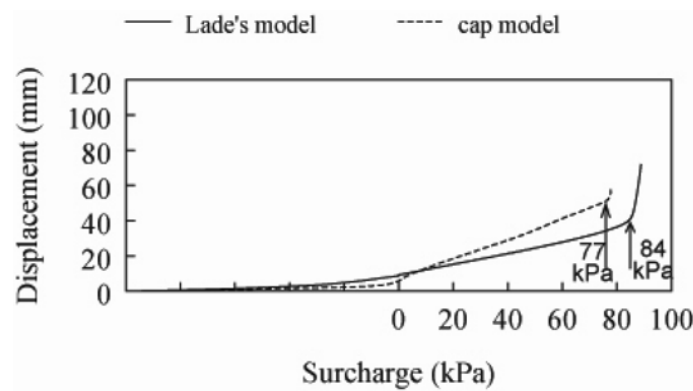
Fig. 7 Lateral displacement at mid-height of facing panel of the RMC wall test: comparison between cap and Lade's models
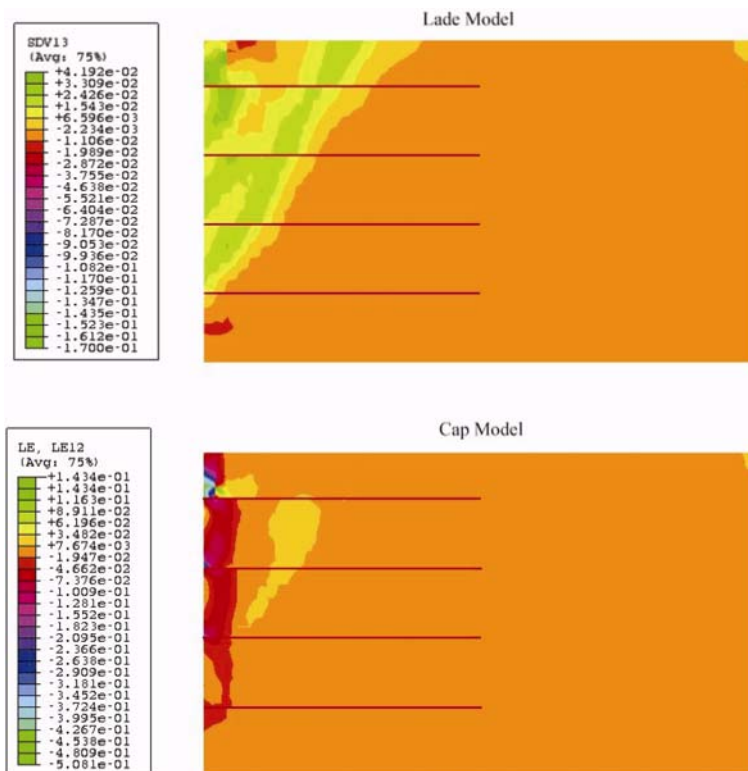

Fig. 8 Shear strain contours of RMC wall at failure: comparison between cap and Lade's models

shown in Fig. 7 for the analyses using the cap model and the Lade's model with Cosserat rotation. The finite element analysis with cap model indicates that failure occurred at a surcharge pressure of approximately 77 kPa as shown in the figure. This is comparable to the at-failure surcharge pressure of 84 kPa predicted by Lade's model with Cosserat rotation. However, the shear strain contours at failure predicted by the cap model, shown in Fig. 8, do not indicate the presence of a failure plane
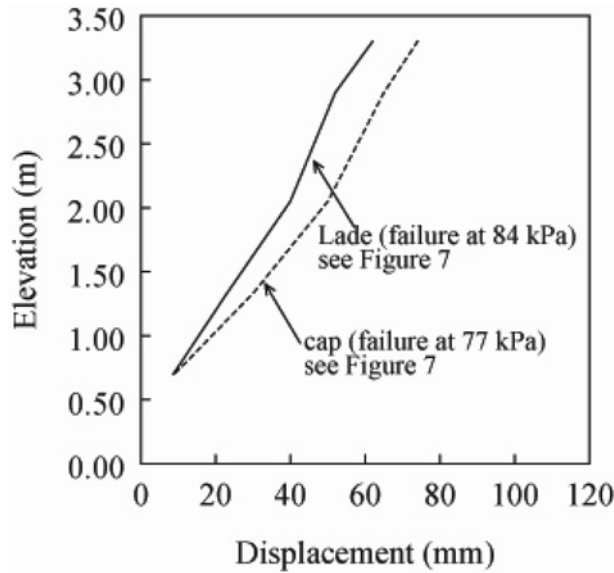
Fig. 9 Lateral displacement of facing panel at failure in the RMC wall test: comparison between cap and Lade's models
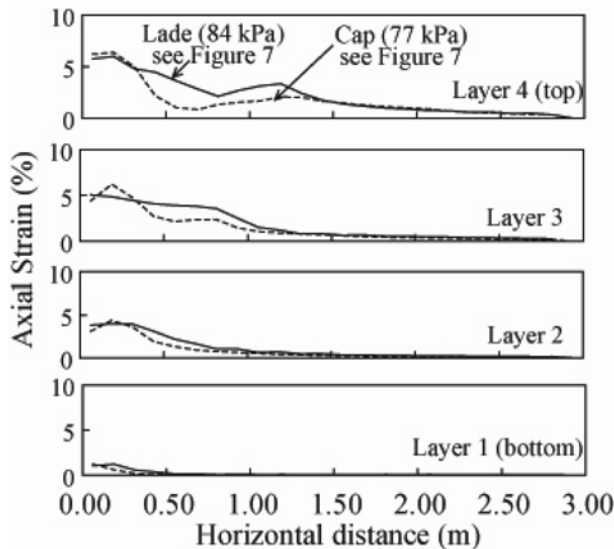

Fig. 10 Axial strain in geogrid layers: comparison between cap and Lade's models

that is clearly present in the case of Lade's model, also shown in Fig. 8, in which a distinct failure plane passing through the heel of the retaining wall and through the reinforced zone is observed. It is clear from Fig. 8 that the predicted at-failure surcharge pressure using the cap model (Fig. 7) is due to premature local shear failures of the soil between the geosynthtic layers adjacent to the soil-wall interface. This type of failure does not agree with the failure plane observed in the RMC test shown in Fig. 3.

Fig. 9 shows the predicted lateral displacements of the facing panel at different heights using both

models. It is noted from the figure that the displacements predicted by the cap model are substantially greater than those predicted by Lade's model even though the displacements predicted by the cap model are taken at a pressure of 77 kPa while the displacements predicted by Lade's model are taken at a greater at-failure pressure of 84 kPa.

Fig. 10 shows comparisons between predicted axial strains in the four reinforcement layers at failure for the two models. It appears that there is a reasonable agreement between the two especially in terms of maximum strains. But a careful look will reveal that the strain distribution predicted by Lade's model is affected by the location of the shear band predicted by this model (i.e. large strains occur at the intersection of the shear band with the geosynthetic layers, Fig. 8).

6. Denver geosynthetic-reinforced soil retaining wall

6.1 Analysis of the Denver wall using Lade's model

The Denver wall test and its testing facility are described in detail by Wu (1992). The reasons for selecting the Denver wall test as a benchmark test are similar to those of the RMC wall test: the Denver wall test is a full-scale test that exhibited distinct failure surfaces through its reinforced zone. The Denver test configuration is simple to analyze since it is in a plane strain condition and has well-defined boundaries, also, the facing of the Denver wall consisted of inter-connected timber logs with plywood packing which is easy to analyze as a continuous beam.

The Denver wall, shown in Fig. 11, is 3 m high, 1.2 m wide and 2.0 m deep. Ottawa sand was
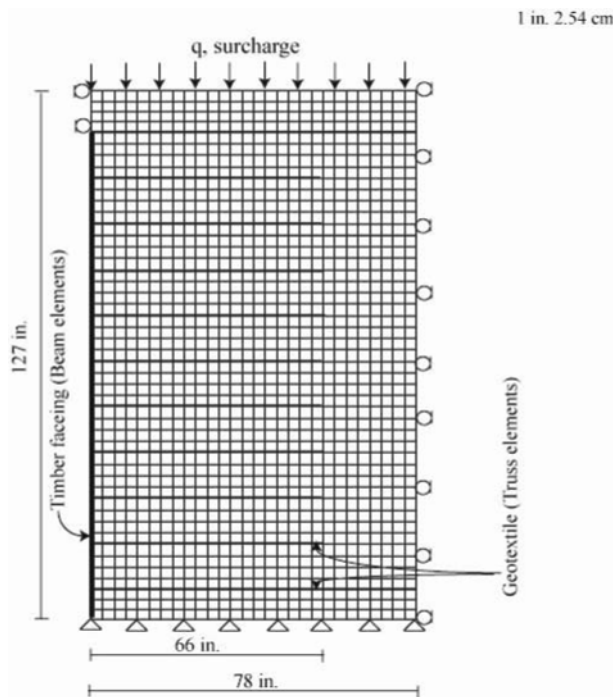

Fig. 11 Finite element mesh of Denver wall

*Mustafa Alsaleh, Akadet Kitsabunnarat and Sam Helwany*
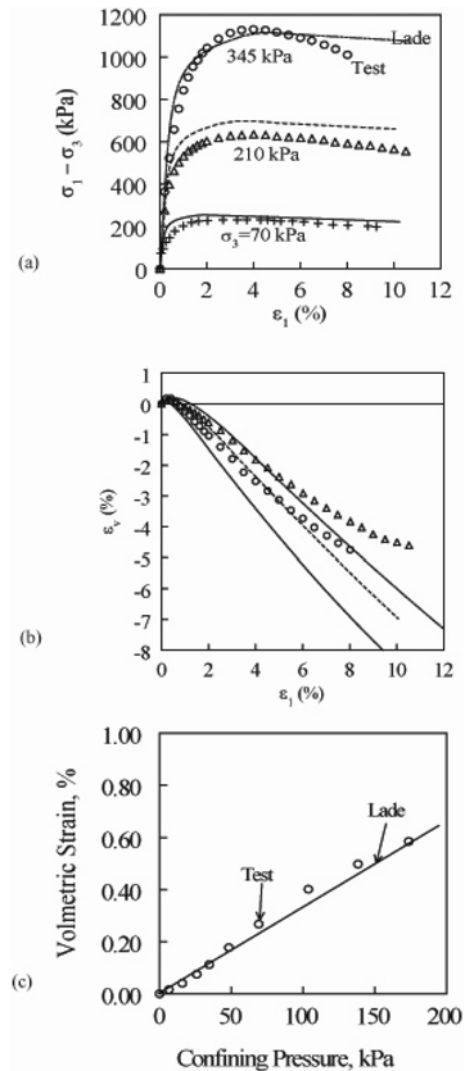
Fig. 12 (a,b) Triaxial test results of backfill sand used in Denver wall; (c) isotropic compression test results of backfill sand used in Denver wall

used as backfill in the test and placed by the air pluviation method in an air-dried condition. A geosynthetic reinforcement was placed at approximately 28-cm vertical spacing. The wall facing comprised inter-connected timber logs with plywood packing. Uniform pressure increments of 35 kPa were applied to the top surface of the backfill soil utilizing a pair of air bags.

The backfill used in the Denver wall was sub-rounded silica Ottawa sand. The specific gravity of the sand was 2.65 and the maximum and minimum unit weights were 17.7 kN/m³ and 15.3 kN/m³, respectively. The placement unit weight was approximately 16.8 kN/m³. Triaxial compression tests results for this sand at confining pressures of 70, 210, and 345 kPa are shown in Figs. 12a and 12b. Isotropic compression test results are given in Fig. 12c.

The reinforcement used in the test was a fairly light weight nonwoven heat-bonded polypropylene

Table 3 Lade's model parameters for Denver wall

Parameter	Value
Failure Criterion	
m	0.13
η_1	45
Elastic Parameters	
M	769
λ	0.182
υ	0.24
Plastic Potential Function	
ψ_2	-2.2
μ	1.1
Work Hardening Law	
C	0.00001
p	1.72
Yield Function	
α	0.5
h	0.47

geotextile with a modulus elasticity of 4.45 kN at 10% elongation, and 60% elongation at break. An elastic modulus of 36 MPa and a shear modulus of 13.9 MPa are estimated for the beam section of the timber facing from the results of a loading test performed by Wu (1992) on a timber/plywood unit supported along two lines at its bottom and subjected to two line loads of equal magnitude.

The timber facing was represented by 2-node beam elements, the geotextile reinforcement was represented by 2-node truss elements, and the soil was represented by a 4-node isoparametric plane strain element with four integration points.

The soil behavior was simulated by Lade's model/Cosserat theory. The model parameters for the sand used in the Denver wall were determined from the results of the triaxial compression tests and the isotropic compression test. These parameters, shown in Table 3, were used to back calculate the triaxial compression tests results. A good agreement between the model simulation and the triaxial test results was obtained, as indicated in Fig. 12.

The calculated and measured lateral displacements at the wall mid height are compared in Fig. 13. The wall is assumed to have failed at the point where the slope of the pressure-displacement curve changes abruptly. The experimental pressure-displacement curve shown in the figure indicates that the failure load is approximately 186 kPa, whereas the predicted pressure-displacement curve indicates a slightly smaller failure load of approximately 169 kPa.

There exist several experimentally detected failure surfaces at failure as shown in Fig. 14a. The calculated shear strain contours at failure, shown in Fig. 14b, clearly illustrate the presence of a failure plane passing through the heel of the retaining wall and also through the reinforced zone. This failure plane compares relatively well with the one measured in Denver test wall (Fig. 14a).

The measured axial strain distributions along the geotextiles at three different elevations of the Denver test wall are compared with the finite element results as shown in Fig. 15. It is noted that the calculated and measured strains are in satisfactory agreement.

It is to be noted that the Denver test wall, shown in Fig. 11, does not represent a typical cross-
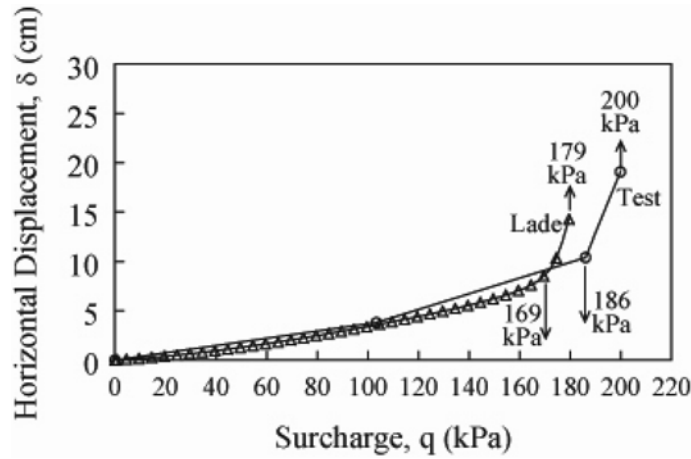
Fig. 13 Horizontal displacements versus surcharge (at mid-height)
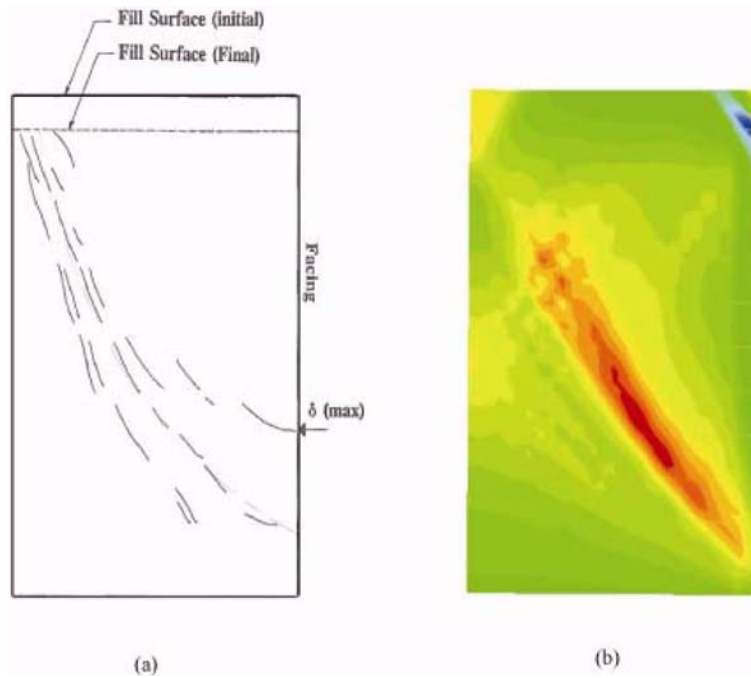

Fig. 14 Failure surfaces: (a) experimental results [After Wu 1992], (b) numerical results

section of a GRS retaining wall because it has very little backfill behind the reinforced soil zone. Hence, the effects of retained soil are nearly excluded. The Denver test wall also restricted the horizontal movement of the top of the facing of the wall. Nevertheless, in the above analysis, the Denver test wall was merely treated as a "boundary value" problem which was utilized to investigate the usefulness of the Lade's model/Cosserat theory embodied in the finite element method. Consequently, the validated code can be utilized, with some confidence, to analyze more realistic GRS retaining wall configurations.
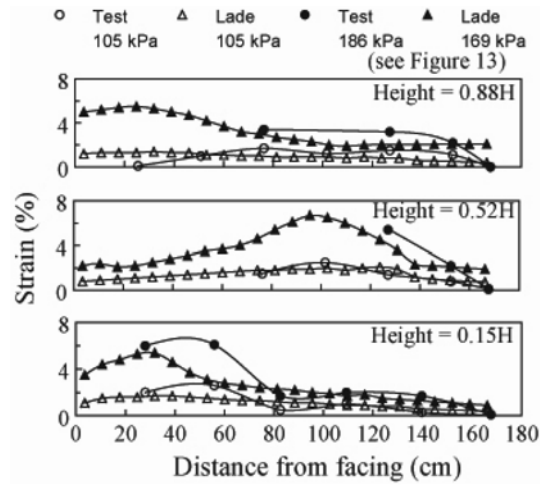
Fig. 15 Axial strain distribution in geosynthetic reinforcements

Table 4 Cap model parameters for Denver wall

Elasticity	Plasticity
E = 172350 kPa	d = 1×10^{-5} kPa
ν = 0.2	β = 57.2° for triaxial condition
	β = 45° for plane strain condition
	R = 0.6
	Initial Yield = 0.0
	α = 0.05
	K = 1

Yield Stress (kPa)	Volmectric Plastic Strain
1.44	0
4.40	0.00005
7.63	0.00006
10.8	0.00008
14.3	0.00009
17.1	0.0001
20.3	0.0002
23.5	0.00025
26.6	0.0003
29.8	0.0004
33.0	0.0005
35.6	0.0006
48.2	0.0007
69.0	0.00125
207	0.0022
345	0.0028
480	0.0032
680	0.00385
780	0.0042

6.2 Analysis of the Denver wall using cap model

To examine the performance of the cap model, the previous analysis of the Denver wall is

repeated in an identical manner but with the cap model used in lieu of Lade's model with Cosserat rotation. The cap model parameters were obtained from three triaxial compression tests and an isotropic compression test results on Ottawa sand. These parameters are given in Table 4. Using one axisymmetric finite element along with these cap model parameters, the results of the three triaxial compression tests and the isotropic compression test were calculated as shown in Fig. 16. The figures indicates good agreement between the cap model and the Lade's model predictions, except for the volumetric strain versus axial strain curves shown in Fig. 16b. This is expected since the cap model is not capable of describing soil dilatancy as indicated earlier.
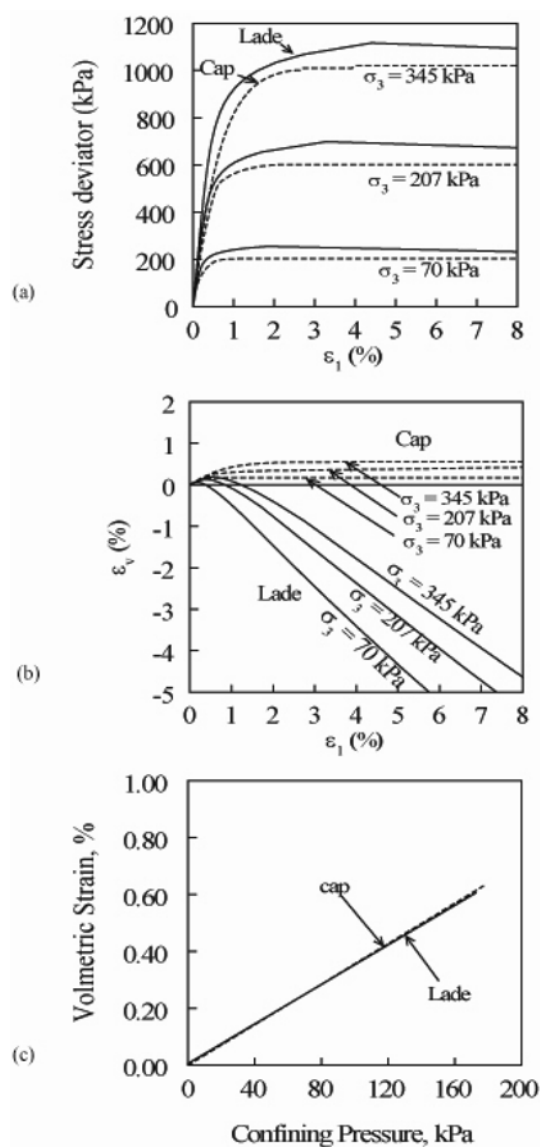

Fig. 16 (a, b) Stress-strain relationship: comparison between cap and Lade's models; (c) isotropic compression test results of backfill sand used in Denver wall
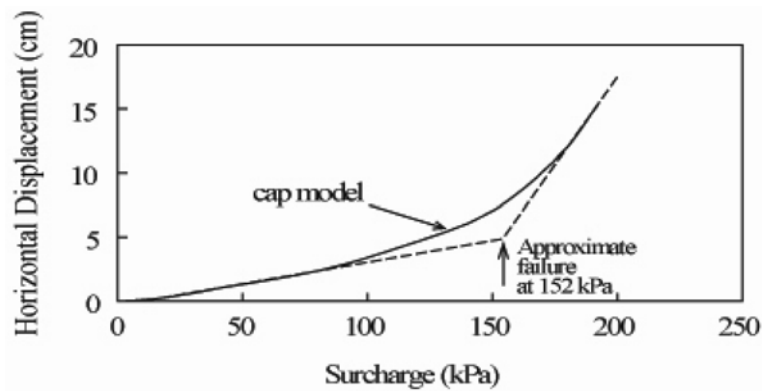
Fig. 17 Horizontal displacement (at mid-height of facing) vs. surcharge for Denver wall using cap model
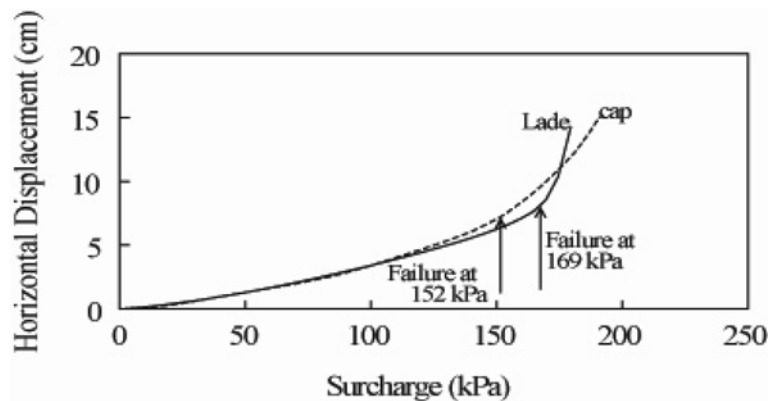

Fig. 18 Horizontal displacement (at mid-height of facing) vs. surcharge: comparison between cap and Lade's models

The calculated lateral displacement at mid-height of the facing panel of the Denver wall test is shown in Fig. 17 for the analyses using the cap model alone, and in Fig. 18 for both the cap model and Lade's model with Cosserat rotation. Fig. 17 indicates that the cap model predicts a "ductile" failure without a distinct failure load. A failure load of approximately 152 kPa is obtained from Fig. 17 using the graphical method illustrated in the figure. In contrast, Lade's model with Cosserat rotation predicts a "brittle" failure at approximately 169 kPa as shown in Fig. 18. Note the well-defined pressure at failure in this figure for Lade's model. The shear strain contours at failure predicted by the cap model, shown in Fig. 19, do not indicate the presence of a failure plane, whereas a clear failure plane is predicted by Lade's model as shown in the same figure. The type of failure predicted by the cap model in Fig. 19 does not agree with the failure plane observed in the Denver wall test (Fig. 14a).

The predicted lateral displacements of the facing panel at different heights using both models are shown in Fig. 20. It is noted from the figure that the displacements predicted by the cap model are quite different from those predicted by Lade's model especially in the upper portion of the facing panel.
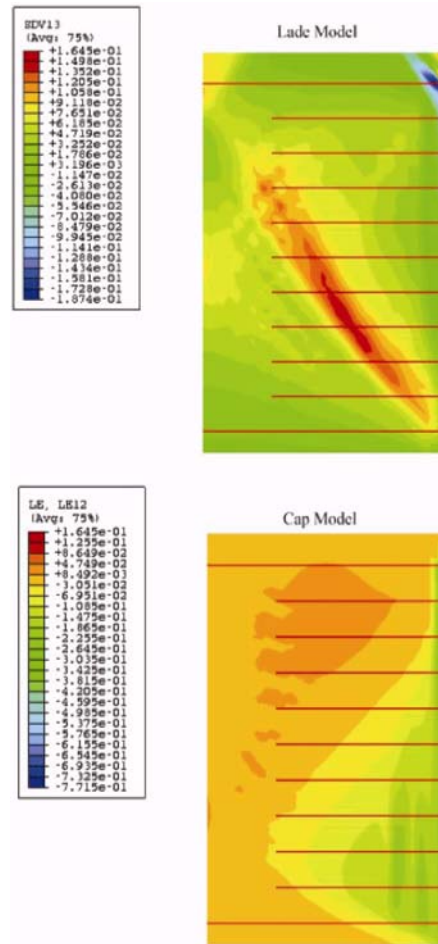
Fig. 19 Shear strain contours at failure of Denver wall: comparison between cap and Lade's models
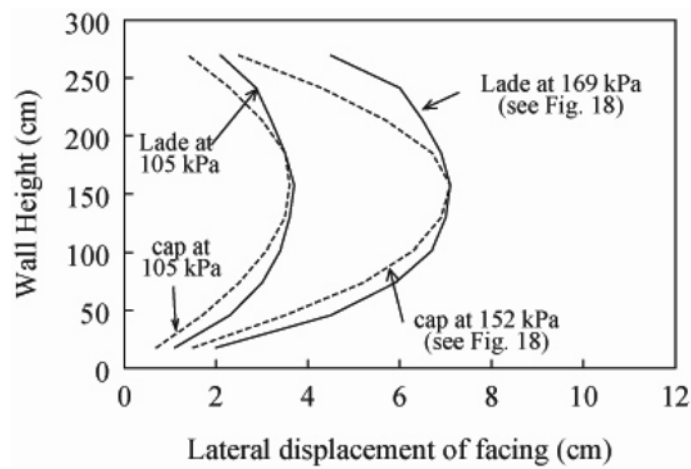

Fig. 20 Lateral displacement at the facing: comparison between cap and Lade's models
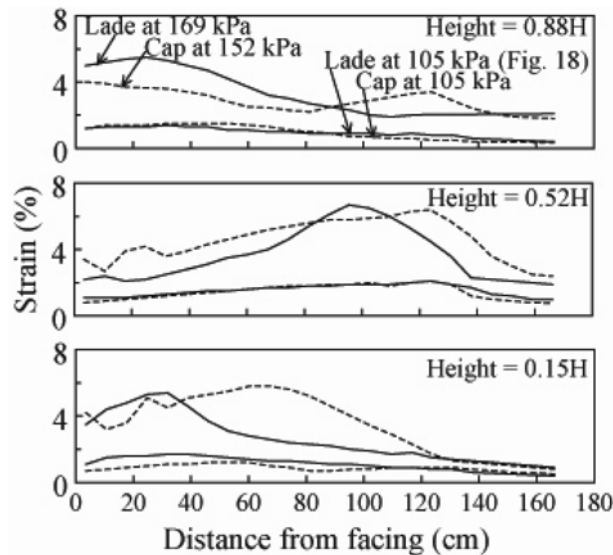
Fig. 21 Axial strain distribution in geotextile reinforcement: comparison between Lade and Cap models

Finally, comparisons between predicted axial strains by the two models in three reinforcement layers are shown in Fig. 21. The at-failure strain distributions predicted by the two models are very different even though their predicted maximum strains are comparable. It is noted from the figure that the strain distribution predicted by Lade's model is affected by the location of the shear band predicted by this model, i.e., higher strains are calculated at the intersections of the shear band with the geosynthetic layers (Fig. 19).

7. Conclusions

Within the framework of finite element, Lade's single hardening model with Cosserat theory was capable of predicting the development of shear banding in the reinforced soil mass behind a GRS retaining wall when the soil mass was subjected to a monotonically increasing surcharge pressure. From the results presented above, the finite element analyses with Lade's model were able to reasonably simulate the large-scale plane strain laboratory tests on geosynthetic-reinforced soil retaining walls. On average, the finite element analyses gave reasonably good agreement with the experimental results in terms of global performances and shear band occurrences. Reasonably accurate prediction of failure loads and shear bands for the RMC wall and the Denver wall were possible using such a soil model.

In contrast, the cap model was not able to simulate the development of shear banding in the RMC wall and the Denver wall. In the RMC wall simulation the cap model predicted a failure load that was substantially less than the measured one. This was attributed to the premature failure of soil elements adjacent to the facing panel. No shear band was detected in this analysis. Also, in the Denver wall simulation the cap model predicted a ductile failure without a distinct failure load. The failure load was graphically estimated from the calculated pressure-displacement curve. The estimated failure load was substantially less than the measured one. Again, no shear band was

detected at failure conditions using this model.

References

Alsaleh, M.I. (2004), *Numerical modeling of strain localization in granular materials using Cosserat theory enhanced with microfabric properties*, PhD thesis, Louisiana State University.

Alsaleh, M.I., Voyiadjis, G.Z. and Alshibli, K.A. (2006), "Modelling strain localization in granular materials using micropolar theory: Mathematical formulations", *Int. J. Numer. Anal. Met. Geomech.*, **30**, 1501-1524.

Alshibli, K.A., Alsaleh, M.I. and Voyiadjis, G.Z. (2006), "Modelling strain localization in granular materials using micropolar theory: Numerical implementation and verification", *Int. J. Numer. Anal. Met. Geomech.*, **30**, 1525-1544

Baladi, G.Y. and Rohani, B. (1979), "An Elastic-Plastic Constitutive Model for Saturated sand Subjected to Monotonic and/or Cyclic Loadings", *Proceedings of the 3rd International Conference on Numerical Methods in Geomechanics*, Aachen, April.

Bathurst, R.J., Wawrychuk, W.F. and Jarrett, P.M. (1987), *laboratory investigation of two large-scale geogrid reinforced soil walls in the application of polymeric reinforcement in soil retaining structures*, Kluwer Academic Publishers, Dordrecht.

Bathurst, R.J. and Benjamin, D.J. (1990), "Failure of a geogrid-reinforced soil wall", *Transport. Res. Rec.*, **1288**, 109-116.

Bauer, E. and Huang, W. (2001), *Influence of density and pressure on spontaneous shear band formations in granular materials*, IUTAM Symposium on Theoritical and Numerical Methods in Continuum Mechanics of Porous Materials, Dordrecht.

Chen, W.F. and McCarron, W.O. (1983), "Modeling of Soils and Rocks Based on Concept of Plasticity", *Proceedings of the Symposium on Recent Developments in Laboratory and Field Tests and Analysis of Geotechnical Problems*, Bangkok.

Cosserat, E. and Cosserat, F. (1909), *Theory des corps deformables*, Herman et fils, Paris.

Daddazio, R.P., Ettouney, M.M. and Sandler, I.S. (1987), "Nonlinear Dynamic Slope Stability Analysis", *J. Geotech. Eng.*, ASCE, **113**(4), 285-298.

Gudehus, G. and Nubel, K. (2004), "Evolution of shear bands in sand", *Geotechnique*, **54**(3), 187-201.

Huang, T.K. and Chen, W.F. (1990), "Simple Procedure for Determining Cap-Plasticity-Model Parameters", *J. Geotech. Eng.*, **116**(3), 492-513.

Huang, W., Nubel, K. and Bauer, E. (2002), "Polar extension of a hypoplastic model for granular materials with shear localization", *Mech. Mater.*, **34**, 563-576.

Kim, M.K. and Lade, P.V. (1988), "Single hardening Constitutive Model for Frictional Materials, I. Plastic Potential Function", *Comput. Geotech.*, **5**, 307-324.

Lade, P.V. and Kim, M.K. (1988), "Single hardening Constitutive Model for Frictional Materials, II. Yield Criterion and Plastic Work Contours", *Comput. Geotech.*, **6**, 13-29.

Lade, P.V. and Nelson, R.B. (1987), "Modelling the elastic behavior of granular materials", *Int. J. Numer. Anal. Met. Geomech.*, **11**, 521-542.

Lai, T.Y., Borja, R.I., Duvernay, B.G. and Meehan, R.L. (2003), "Capturing strain localization behind a geosynthetic-reinforced soil wall", *Int. J. Numer. Anal. Met. Geomech.*, **27**, 425-451.

McCarron, W.O. and Chen, W.F. (1987), "A Capped Plasticity Model Applied to Boston Blue Clay", *Can. Geotech. J.*, **24**(4), 630-644.

Minuzo, E. and Chen, W.F. (1984), "Plasticity Modeling and its Application to Geomechanics", *Proceedings of the Symposium on Recent Developments in Laboratory and Field Tests and Analysis of Geotechnical Problems*, Rotterdam.

Nelson, I. and Baladi, G.Y. (1977), "Outrunning Ground Shock Computed with Different Methods", *J. Eng. Mech-ASCE*, **103**(3), 377-393.

Pasternak, E. and Mühlhaus, H.B. (2002), "Large deformation Cosserat continuum modeling of granulate materials", *Proceedings of the 3rd Australasian Congress on Applied Mechanics*, Sydney.

Rubin, M.B. (2000), *Cosserat Theories: Shells, Rods, and Points (Solid Mechanics and Its Applications)*,

Springer Netherlands.

Tejchman, J. and Bauer, E. (1996), "Numerical Simulation of Shear Band Formation with a Polar Hypoplastic Constitutive Model", *Comput. Geotech.*, **19**(3), 221-244.

Tomantschger, K.W. (2002), "A boundary value problem in the micropolar theory", *Zamm-Z. Angew. Math. Me.*, **82**(6), 421-422.

Vardoulakis, I. and Sulem, J. (1995), *Bifurcation Analysis in Geomechanics*, Routledge.

Wu, J.T.H. (1992), "Predicting performance of the Denver walls", *General Report*, Denver.